Synchrotron radiation-based far-infrared spectroscopic ellipsometer with full Mueller-matrix capability

T. N. Stanislavchuk,[1,a),b)] T. D. Kang,[1,a)] P. D. Rogers,[1] E. C. Standard,[1] R. Basistyy,[1] A. M. Kotelyanskii,[1,2] G. Nita,[1] T. Zhou,[1] G. L. Carr,[3] M. Kotelyanskii,[1,4] and A. A. Sirenko[1]
[1]*Department of Physics, New Jersey Institute of Technology, Newark, New Jersey 07102, USA*
[2]*Allegheny College, Meadville, Pennsylvania 16335, USA*
[3]*National Synchrotron Light Source, Brookhaven National Laboratory, Upton, New York 11973, USA*
[4]*Rudolph Technologies Inc., Flanders, New Jersey 07836, USA*

(Received 11 November 2012; accepted 14 January 2013; published online 5 February 2013)

We developed far-IR spectroscopic ellipsometer at the U4IR beamline of the National Synchrotron Light Source in Brookhaven National Laboratory. This ellipsometer is able to measure both, rotating analyzer and full-Mueller matrix spectra using rotating retarders, and wire-grid linear polarizers. We utilize exceptional brightness of synchrotron radiation in the broad spectral range between about 20 and 4000 cm^{-1}. Fourier-transform infrared (FT-IR) spectrometer is used for multi-wavelength data acquisition. The sample stage has temperature variation between 4.2 and 450 K, wide range of θ–2θ angular rotation, χ tilt angle adjustment, and X-Y-Z translation. A LabVIEW-based software controls the motors, sample temperature, and FT-IR spectrometer and also allows to run fully automated experiments with pre-programmed measurement schedules. Data analysis is based on Berreman's 4×4 propagation matrix formalism to calculate the Mueller matrix parameters of anisotropic samples with magnetic permeability $\mu \neq 1$. A nonlinear regression of the rotating analyzer ellipsometry and/or Mueller matrix (MM) spectra, which are usually acquired at variable angles of incidence and sample crystallographic orientations, allows extraction of dielectric constant and magnetic permeability tensors for bulk and thin-film samples. Applications of this ellipsometer setup for multiferroic and ferrimagnetic materials with $\mu \neq 1$ are illustrated with experimental results and simulations for $TbMnO_3$ and $Dy_3Fe_5O_{12}$ single crystals. We demonstrate how magnetic and electric dipoles, such as magnons and phonons, can be distinguished from a single MM measurement without adducing any modeling arguments. The parameters of magnetoelectric components of electromagnon excitations are determined using MM spectra of $TbMnO_3$. © *2013 American Institute of Physics*. [http://dx.doi.org/10.1063/1.4789495]

I. INTRODUCTION

Optical spectra of complex materials, such as magnetoelectric (ME) and multiferroic (MF) crystals, materials with chirality, and metamaterials, are in the focus of modern experimental and theoretical studies. The complex materials can reveal a so-called *bi-anisotropic* optical behavior in a form of the fascinating effects, such as nonreciprocal light propagation, negative index of refraction, and polarization plane rotation.[1] These exotic optical phenomena are not limited, but are usually expected to occur in the far-IR part of the optical spectrum, which is dominated by elementary excitations, such as optical phonons, magnons, electromagnons, and crystal field transitions. The common feature of these complex materials is that their properties cannot be correctly represented only with a dielectric susceptibility tensor $\hat{\varepsilon}(\omega)$ and a number of additional functions, such as the magnetic permeability $\hat{\mu}(\omega)$ and ME $\hat{\alpha}(\omega)$ tensors should be included into consideration. As a result, a single transmission or reflection spectrum cannot properly describe the entangled contribution of $\hat{\varepsilon}(\omega)$, $\hat{\mu}(\omega)$, and $\hat{\alpha}(\omega)$ to the optical behavior of bi-anisotropic materials. Instead, a combination of the adequate theoretical description and advanced experimental spectroscopic techniques is required to achieve an understanding of complex materials. As we demonstrate in this paper, the theoretical representation of bi-anisotropic phenomena can be done with the help of the Mueller matrices (MM). Correspondingly, one of the most efficient experimental techniques for studies of elementary excitations in bi-anisotropic materials is Mueller matrix spectroscopic ellipsometry (MM-SE), which can be realized in reflection and transmission configurations with variable azimuthal angle and variable angle of incidence (AOI).

To support extensive research efforts for studies of complex materials, a multiuser facility for MM-SE has been designed, developed, and installed at the National Synchrotron Light Source, Brookhaven National Laboratory (NSLS-BNL). The new ellipsometer covers the spectral range between 20 and 4000 cm^{-1}. Several sets of rotating retarders enable a full Muller matrix analysis of anisotropic and bi-anisotropic samples. The typical spot-size of about 3×3 mm^2 at the sample position for the slowly focused synchrotron radiation with $f_{\#} = 20$ allows studying relatively small samples with the surface area of about 1×1 mm^2. In this paper we will describe the instrument in details and will present several examples of the measured rotating analyzer ellipsometry (RAE) and MM spectra of magnetic and ME materials such as $Dy_3Fe_5O_{12}$ and $TbMnO_3$ single crystals. The experimental

[a)]T. N. Stanislavchuk and T. D. Kang contributed equally to this work.
[b)]Electronic mail: stantar@njit.edu.

spectra have been simulated and fitted using 4 × 4 Berreman's matrix formalism. The related activity of our team in theory of the data analysis and simulations in materials with $\mu \neq 1$ is published in Ref. 2. The principles of the rotatable broadband optical retarders are published in Ref. 3. Several important aspects for analysis of the optical spectra for samples with the magnetic permeability $\mu \neq 1$ are summarized in Ref. 4. Examples of our recent RAE measurements are in Refs. 5 and 6.

II. INSTRUMENTATION

A. Importance of the synchrotron radiation for far-IR ellipsometry

Synchrotron radiation (SR) based far-IR spectroscopic ellipsometry is a versatile technique for materials studies, which has been developed at several SR facilities. The first ellipsometry experiments at NSLS-BNL, which began in the mid 90s, had been initiated in early 90s at the former Department of Solid State Spectroscopy headed by M. Cardona in the Max-Planck-Institute für Festkörperforschung (MPI-FKF). The design of the first generation of the far-IR ellipsometer for SR measurements was described by Kircher *et al.*[7] and Henn *et al.*[8] The first instrument was designed and assembled at MPI-FKF and then installed at NSLS-BNL. The MPI-FKF ellipsometer was equipped with a rotating analyzer and a stationary retarder. The spectroscopic ellipsometry activity at NSLS-BNL reached its peak between 1997 and 2002, as reflected in a number of publications by Bernhard *et al.*[9–12] After 2003, the ellipsometry activity in the field of strongly correlated systems and high-temperature superconductivity was transferred from NSLS to ANKA, Forschungszentrum, Karlsruhe, Germany.[13–21] The design of the far-IR ellipsometer at ANKA, which is similar to that of MPI-FKF, is described in Ref. 22.

Another approach to THz ellipsometry at the synchrotron source was described by Röseler *et al.*[23] That ellipsometer is based on a Martin-Puplett (MP) interferometer. All Stokes parameters of the polarized light can be determined without the need of a retarder as a phase shifting device. This setup has been tested below 1.5 THz employing synchrotron radiation at BESSY from a bending magnet as a dipole radiation source. Application of MP interferometers for ellipsometry is a novel instrumentation approach, which certainly has a potential for the THz spectral range below 100 cm^{-1} due to its higher resolution and greater sensitivity over that of the Michelson interferometer.[24] Nevertheless, the approach using the MP interferometer is still suffering from a relatively narrow bandpass of $\Delta\lambda/\lambda \approx 0.1$ due to the spectral imperfection of the wire grid polarizer as the beam splitter in the interferometer. Its implementation at the typical optical phonon frequencies of oxide crystals 200–700 cm^{-1} is quite difficult due to the mechanical limits imposed by the alignment requirements for the moving mirrors of a MP interferometer.[25]

The research group of M. Schubert initiated another interesting SE program at BESSY II, Berlin, Germany. The first ellipsometer setup capable of doing measurements in the external magnetic field using SR was described by Hofmann *et al.*[26] This ellipsometer employed both RAE and truncated measurements of the 3 × 3 upper left block of normalized MM in the spectral region from 30 to 650 cm^{-1}.

B. U4IR beamline and the properties of the light source

Our new ellipsometer was installed in 2010 at U4IR beamline of the NSLS VUV-IR electron storage ring. This beamline specializes in the development of new instrumentation for eventual implementation at operating IR beamlines, including for microscopy, high-field magnetospectroscopy, beam stabilization, and ellipsometry. The characteristics of the light at the U4IR beamline define many of the ellipsometer's spectroscopic capabilities. The infrared light, produced as dipole bending magnet radiation, is extracted from the storage ring through an aperture that collects an angular range of 90 mrad vertical by 90 mrad horizontal. The collected beam is transported by an optical system based on a pair of matched ellipsoidal mirrors that produce a 1:1 image of the source at a wedged diamond window. This window isolates the UHV synchrotron environment from the rough vacuum of the spectrometer and other instruments. The 90 mrad extraction and 11 mm diameter aperture of this diamond window perform optimally from the visible to 0.4 mm wavelengths (25 cm^{-1}) in the far-IR. Performance at longer wavelengths drops rapidly due to diffraction losses.

The infrared synchrotron radiation from the diamond window is collimated and transported to a Bruker IFS 66v FT-IR spectrometer with a full complement of beamsplitters to span the spectral range from far-IR to visible light. The best available spectral resolution of the installed spectrometer is 0.3 cm^{-1}. From here the IR radiation is sent to the ellipsometer. The exceptional brightness of the synchrotron light source exceeds that for a conventional thermal light source (T = 1200 K) by a factor of 1000 for wavelengths longer than 10 μm where the source has diffraction-limited dimensions.[27] This is crucial for throughput-limited techniques such as microscopy and ellipsometry. For microscopy, optics with a large numerical aperture (NA) of about 0.6 can be used to focus light to a spot just a few wavelengths in size. In contrast, ellipsometry requires a well-defined AOI on the sample such that the NA is limited to much smaller values of less than 0.05. Thus the diffraction-limited spot onto the sample is nearly 50λ and the instrument's throughput is diffraction-limited at 50 cm^{-1} (λ = 200 μm) for even a 10 mm-size sample. The situation becomes even more challenging when a large AOI is needed for good ellipsometric sensitivity to, for example, a strong metallic response of the sample. Preparing large, high quality samples can be challenging, so effectively all far-infrared ellipsometry measurements have very low throughput. As demonstrated by Kircher *et al.*,[7] high brightness synchrotron radiation overcomes this throughput limit and allows for relatively quick ellipsometric measurements of the samples with a modest cross section area of a few mm^2. This capability has become increasingly important for researching complex oxides where competing orders drive new physical phenomena (e.g., superconductivity, colossal magnetoresistance, multiferroicity). Understanding these materials

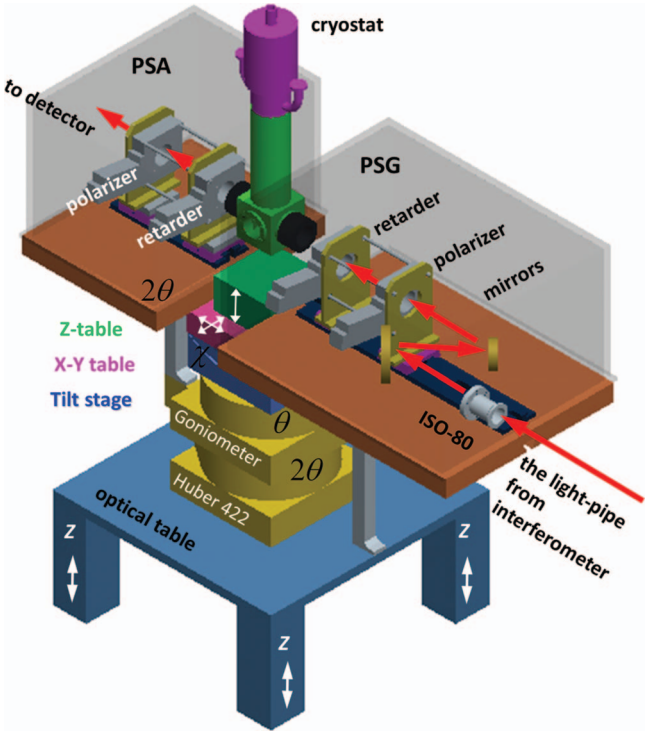

FIG. 1. Ellipsometer at U4IR beamline consists of three major components: Polarization state generation (PSG) section, sample stage with an optical cryostat, and polarization state analyzer (PSA) section. Straight red arrow shows light propagation direction from the interferometer towards ellipsometer. Sample stage and PSA section can rotate around the same vertical axis to accommodate the ellipsometric measurements at different AOIs.

can require probing the multi-dimensional parameter space of temperature, external electric field, pressure, and orientation (e.g., for anisotropic crystals); a potentially impractical measurement task without access to the rapid data collection rates at the synchrotron radiation facilities. For example, using this ellipsometer at U4IR, a complete measurement of the temperature dependent pseudo dielectric function for one sample orientation can be accomplished in less than one day.

C. General design

Figure 1 shows a general schematics of the ellipsometer at U4IR beamline, which consists of several major sections: (i) polarization state generator (PSG), (ii) sample section with a cryostat, θ-2θ, tilt angle χ, and X-Y-Z motorized translation stages, and (iii) polarization state analyzer (PSA). Far-IR and mid-IR synchrotron radiations from the storage ring pass through an FT-IR spectrometer (not shown in Fig. 1). After that the radiation enters the PSG chamber, which is equipped with the focusing optics and three motorized rotational stages that hold two linear polarizers and a retarder. The focused radiation with a known state of polarization is reflected from the sample mounted on a cold finger inside an optical cryostat in the sample section. Then, the reflected light from the sample enters PSA, which is equipped with motorized stages for the optical retarder and a linear polarizer. Finally, the analyzed radiation is focused on a detector (not shown in Fig. 1) using a parabolic mirror. The detector is connected to the FT-IR spectrometer. The ellipsometric spectra are measured one after another for fixed position of optical polarizers and retarders.

D. Vacuum components

To minimize the effects of the light absorption in the atmosphere, the optical path for the entire system that includes the FT-IR interferometer, ellipsometer, and detector is under raw vacuum of about 1 Torr provided by three vacuum pumps. A number of gate valves allows for a temporary separation between different vacuum sections of the setup for independent service and exchange of the beamsplitters in the FT-IR spectrometer and optics components in the PSG and PSA chambers. A manifold allows for an independent vacuum control of each ellipsometer section. An optical cryostat is connected to a turbo-pump station (TSU 065D, Pfeiffer Vacuum), which provides cryogenic vacuum of about 10^{-6} Torr in the sample volume.

E. Optical windows

A pair of optical windows separates three sections of ellipsometer: PSG, sample stage, and PSA. The stationary cryostat windows, which are mounted on the walls of PSG and PSA sections, have a permanent orientation with respect to the direction of the light beam for variable AOIs. We use the same primary window material as in the MPI-FKF and ANKA ellipsometers: 6 μm-thick Mylar film. This material is obviously very fragile and cannot sustain a differential pressure of 1 atm or 760 Torr. The Mylar windows require simultaneous vacuum pumping on both sides down to about 1 Torr at all three PSG, sample, and PSA sections of ellipsometer. When the pressure of 1 Torr is achieved on both sides of the same window, then the sample section can be safely pumped down to the cryogenic background pressure of 10^{-6} Torr with no damage to the Mylar windows. Flexible bellows, which are used as connectors between PSG, sample stage, and PSA, allow changes for the AOI in the range of $\pm 7^{\circ}$ at low temperatures and without breaking the vacuum in the sample stage. A set of four different cryostat shrouds is used interchangeably for a broader range of AOIs between 50° and 90°. The latter corresponds to polarimetry measurements in transmission configuration. Mylar as a window material has excellent transmission characteristics below 700 cm^{-1}. There are several known absorption bands in Mylar above 700 cm^{-1}, but most of them do not strongly affect the ellipsometric measurements due to self-normalization procedures in the data analysis except for the strong band at $\sim$3000 cm^{-1}. A set of KRS5 windows, which are free from absorption bands above 450 cm^{-1} can be used in the ellipsometers for the far-IR and especially in mid-IR spectral range.

F. Sample stage

The quality of ellipsometric measurements greatly depends on stability, reproducibility, alignment capability, and position control of the sample inside the setup, which is

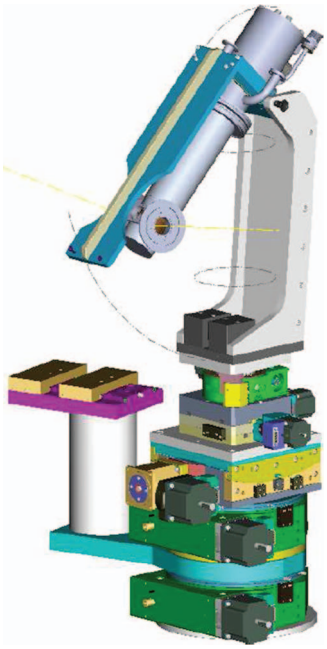

FIG. 2. Schematics of the sample stage and the closed-cycle cryostat assembly. From the bottom to the top, this assembly consists of (i) 2θ-circle with a holder for the PSA chamber, (ii) θ-circle that supports the following, (iii) χ angle adjustment stage with the travel range of $\pm 7^{\circ}$, (iv) X-Y-Z stage, and (v) a closed-cycle cryostat that is shown in the sample-loading position.

provided by the θ-2θ, χ, and X-Y-Z motorized mechanical stages (see Fig. 2). The 2θ arm on the left is supporting the PSA section, which is not shown in Fig. 2. The sample stage allows for an automatic control for the AOI during measurements and calibration procedures. The X-Y-Z motorized stages have a broad range of ± 10 mm for the sample displacements that allows to accommodate single crystals of different size and shape. The stable mechanical design provides reproducibility of the sample motion that is comparable to the requirements acceptable in such precise techniques as, for example, high resolution x-ray diffraction. The sample stage has been designed using standard HUBER components (X-Z translation - 5102.20, Y translation - 5103.2, χ tilt - 5202.8, and θ-2θ rotation - 422 Series) and has a single unit controller for computer communication with the instrument.

G. Cryogenic design and operations

Studies of the phase transitions in strongly correlated materials and multiferroics usually require low temperatures for the sample. For that purpose, the sample stage of the ellipsometer can accommodate one of the two cryostats, a LHe-flow (custom built, OXFORD Instruments) or a closed-cycle one (DE-204SF, ARS Inc.), which can be used interchangeably for the sample cooling down to LHe temperatures. Both cryostats belong to the "cold-finger" type with the sample positioned in high vacuum. The sample is mounted on a 4 mm-diameter holder and is surrounded by two cold copper shields with holes for the light access. By design, no cold optical windows are used in the cryostats. The sample temperature is measured with Si-diode sensors connected to either OXFORD ITC-503 or Lakeshore 340 temperature controllers, which are integrated into the LabVIEW-based experiment control program.

The closed-cycle system allows sample temperature variation between 6 and 450 K. This system does not require LHe and the cooling power is provided with a He gas compressor. The initial cooling time from 300 K to 6 K is about 3 h. Figure 2 shows the closed-cycle cryostat in the sample loading position on top of the XYZ-2-circle-goniometer assembly. This design allows for the sample exchange time to be less than 10 min excluding, of course, the warm-up, pump-down, and cool-down time intervals. One of the disadvantages of the closed-cycle system is related to mechanical vibrations that are transmitted from the compressor to the bolometer through the metal parts of ellipsometer. These vibrations result in a significant noise on the bolometer in the low-frequency range that can be detrimental for ellipsometric measurements of weak signals. An effective solution to this problem includes a combination of both (i) a high scanning speed of the Bruker spectrometer above 80 kHz and (ii) application of an external high-pass electronic filter between the bolometer output and the detector input for the FT-IR spectrometer. If both of the above applied, the ellipsometry spectra can be measured in the broad frequency range above 50 cm^{-1} with unnoticeable disturbance from the He compressor.

The continuous LHe flow system allows for the cold-finger temperature variation between 4 K and 300 K. The cooling power is provided with a LHe flow through a transfer line. The initial cooling time from 300 K to 5 K is about 0.5 h. The LHe consumption is between 5 and 10 liters per experimental day. The LHe flow system is free of vibrations and is preferable for measurements of small samples in the far-IR spectral range below 100 cm^{-1}.

III. LINEAR POLARIZERS, RETARDERS, AND LIGHT FOCUSING

The starting conditions for light focusing are the following: the synchrotron beam is about 40 $\times$ 20 mm^2 and is elongated in vertical direction after exiting the FT-IR spectrometer. A single off-axis parabolic mirror in a combination with two other flat mirrors is used for the light focusing on the sample (see Fig. 3). This beam is focused with $f_{\#} = 20$. Since the light source at U4IR is diffraction-limited in the spectral range below 1000 cm^{-1}, our ellipsometer provides a relatively small spot size of about 3 $\times$ 3 mm^2 at the sample position without intensity-reducing apertures. A high $f_{\#} = 20$ is needed to (i) minimize the uncertainty of the polarization state across the light beam after passing through a retarder and (ii) minimize the uncertainty in the value of AOI at the sample surface. In Ref. 3 we demonstrated that if fast focusing with $f_{\#} < 10$ is used, then the state of polarization after passing an optical retarder has a significant uncertainty that may result in detrimental errors in MM-SE experiments.

To support the full-Muller matrix analysis of polarization, one needs a possibility to obtain several linearly independent states of polarization using both, rotating linear polarizers and rotating retarders. PSG section, as shown in

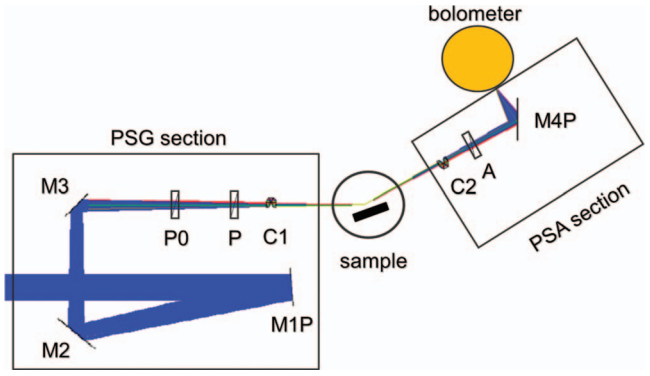

FIG. 3. Schematics of the light propagation between the PSG and PSA sections of the ellipsometer. PSG section consists of a retarder C1, two linear polarizer, P0 and P, and three mirrors: an off-axis parabola M1P with effective focus length of 1 m and two flat ones, M2 and M3. PSA section consists of a retarder C2, analyzing polarizer *A*, and a parabolic mirror M4P for light focusing on a bolometer or a CuGe detector.

Fig. 3, is equipped with two linear polarizers and one retarder. The first linear polarizer *P*0 is used to attenuate and/or purify the polarization of the synchrotron radiation, which is predominantly polarized in vertical direction. The second linear polarizer *P* creates a linear polarization on the sample in RAE measurements or on the retarder in MM-SE measurements. The retarder *C*1 converts a linear polarization into an elliptical (or circular) polarization, which is focused on a sample. After reflection from the sample, radiation enters the PSA section. Retarders and polarizers in PSG and PSA are symmetrically positioned with respect to the sample. All linear polarizers have 25 mm clear aperture. Rotation of both, linear polarizers and retarders is facilitated by HUBER 409 rotational stages. To cover the broad spectral range between 20 and 4000 cm^{-1} we are using interchangeably the following three sets of polarizers:

(i) Free-standing wire-grid linear polarizers from *SPECAC* are used for the frequency range below 200 cm^{-1}. The extinction ratio is between 1:2000 at low frequencies and 1:800 at high frequencies. This extinction ratio is achieved by using "tandems" in both PSA and PSG stages. Above 200 cm^{-1}, the extinction ratio for the free-standing polarizers decreases well below 1:800 due to diffraction, which is not acceptable for accurate RAE and MM-SE experiments.

(ii) Wire-grid polarizers on polyethylene substrates from *Tydex* are used for the frequency range between 30 and 700 cm^{-1}. The extinction ratio is also between 1:2000 and 1:800. The high-frequency cutoff is determined by absorption in the polyethylene substrates.

(iii) Wire-grid linear polarizers from *SPECAC* on KRS5 substrates. The extinction ratio better than 1:800 can be achieved in the frequency range between 450 and 4000 cm^{-1}.

In order to compensate the effect of possible imperfection of polarizers along their surface (the extinction ratio may be slightly different for different parts of the polarizer) the alignment of the beam before the measurements is performed with the apertures placed at the centers of the polarizers. Broadband rotating retarders for the THz and far-IR spectral ranges are not commercially available. We developed several types of rotating retarders based on triangular prisms or double Fresnel rhombs. Preliminary results of this development effort were published in Ref. 3. Multiple conditions have been met in this design, such as (i) a reasonably high transmission in the operating frequency range and (ii) minimal displacement of the beam caused by the 360° retarder rotation around its optical axis.

Figure 4 shows two schematics for the Si prism and KRS5 double Fresnel rhomb retarders. The Si retarder is based on a single 45° prism with 10 × 10 mm^2 acceptance area and three 15 × 15 mm^2 gold mirrors. The retardation of such retarder, which occurs inside Si due to total internal reflection, is about $\Delta \approx 85°$ in the far-IR spectral region, which is different from the ideal theoretical value of $\Delta = \pi/2$ for a single 42° Si prism. Three gold mirrors practically do not change the polarization and intensity of radiation and allow to keep the light beam direction the same before and after the retarder. Rotation of the retarder around its optical axis by 45° allows to change the phase shift between *p*- and *s*-polarized components of the light incident on the sample between 0° (linearly polarized light) and 90° (nearly circular polarized light). Experimental spectra for $\Delta(\omega)$ and $\Psi(\omega)$ of our Si and KRS5 retarders are shown in Fig. 5. Note that due to strong multi-phonon absorption in Si prisms, the spectral range between 450 and 1400 cm^{-1} is excluded from a broad 20–4000 cm^{-1} operational range for the Si retarder. The intensity attenuation factor for Si retarder is about 3 due to reflection and absorption in Si. The brightness of the synchrotron radiation is high enough to compensate these losses. Previously we presented the experimental data for an alternative design of Si retarders based on Si double Fresnel rhomb.[3]

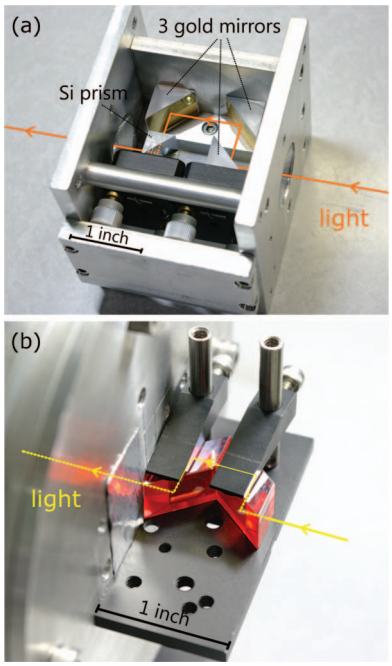

FIG. 4. (a) Rotating retarder based on a single silicon prism and three gold mirrors (4 bounces). (b) Rotating retarder based on two adjacent KRS5 Fresnel rhombs (4 internal bounces). Direction of the light propagation is shown with arrows.

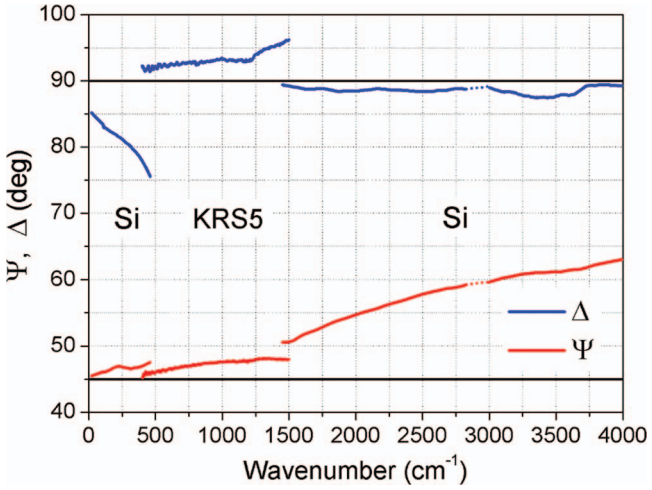

FIG. 5. Experimental spectra for $\Psi(\omega)$ and $\Delta(\omega)$ of Si and KRS5 retarders measured for the retarder position that corresponds to the maximum value of retardation. Black horizontal lines correspond to the theoretical values of $\Psi(\omega)$ and $\Delta(\omega)$ for an ideal retarder. The narrow spectral range around 3000 cm^{-1} is shown with dotted lines due to strong absorption in the Mylar windows.

In spite of its more elegant and compact design, we do not implement this type of Si retarders for MM-SE measurements due to unacceptably high displacement of the transmitted light upon the retarder rotation. Such retarder design would require either very high precision for the surface polishing or a split into two separate rhombs to facilitate their independent alignment. Note that the prism design of the Si retarder provides a much better performance compared to previously described TOPAS retarder in Ref. 3.

To cover the spectral window between 450 and 1400 cm^{-1} we implemented the retarder based on two KRS5 Fresnel rhombs [see Fig. 4(b)]. The split design allows for the independent alignment of two rhombs that is crucial for keeping the direction of the transmitted beam unchanged upon rotation of the retarder around its optical axis. KRS5 retarders pass more than 50% of light. Among disadvantages of the KRS5 retarder is a strong dispersion of $\Delta(\omega)$ above 1500 cm^{-1}. In the nearest future we consider replacing KRS5 retarders with ZnSe or Ge rhombs that should be free from internal defects that cause a strong dispersion of $\Delta(\omega)$ in KRS5.

IV. EXPERIMENT CONTROL SOFTWARE AND THEORY OF OPERATIONS

Standard operations of the ellipsometer setup require a full computer control of the sample position with respect to the beam, sample temperature, as well as the position of the PSA section with respect to the sample, and the position of each polarizer and each retarder. A graphical user interface program for instrument control, calibration, and data acquisition has been developed in the National Instruments' LabVIEW (Laboratory Virtual Instrumentation Engineering Workbench) graphical programming platform. Measurements can be done in a manual regime as well as using text-based schedules that may be used to implement unlimited number of internal loops and timed events. The main program has a capability of analyzing information about the NSLS ring current and pause the measurements during the beam interruption or injection. The LabVIEW protocol-enabled communication between the user's computer and the local computer for FT-IR interferometer allows a possibility to use different models of interferometers. The open code of this program enables a possibility for the future users of the instrument to upgrade and modify this program including the addition of new components, such as external lasers, high electric field, etc.

Traditional Mueller polarimeters for the near-IR, visible, and UV wavelength ranges use different ways of controlling and measuring polarization state: liquid crystal-based devices, that modulate retardation by switching the orientation of the fast axes of the retardation, coupled acousto- or electro-optical modulators, or by rotating polarizers and birefringent retarders. Unfortunately, none of these options is available in the far-IR range. In our system the polarization states in the PSA and PSG are selected by rotating the retarders, and polarizers around the optical axis. Using FT-IR spectrometer makes continuously rotating retarders or polarizers impractical, and polarization states of the PSA and PSG are selected from the discrete set of states, that can be specified in the LabVIEW program schedule.

Measurement of the Mueller matrix of the sample at each incidence angle, or sample orientation, will include collecting the reflected light intensity spectra at different combinations of azimuthal angles of the polarizer P, and retarder $C1$ in the PSG, and the second retarder $C2$, and analyzing polarizer A in the PSA. These orientations comprise a set of $\{P,C1,C2,A\}$ instrument states sampled in a Mueller matrix measurements.

Light intensity at the detector I_{det} is the first component of the Stokes vector, characterizing the light incident at the detector $\vec{S}_{\text{det}}$, which is given by the following equation:

$$\begin{aligned} &I_{\text{det}} = [1 \quad 0 \quad 0 \quad 0]\,\vec{S}_{\text{det}};\\ &\vec{S}_{C1} = \hat{C}(C1)\hat{P}(P)\vec{S}_{\text{inc}};\\ &\vec{S}_{\text{det}} = \hat{P}(A)\hat{C}(C2)\hat{M}_S\vec{S}_{C1} = \hat{A}\hat{M}_S\vec{S}_{C1};\\ &\hat{A} = \hat{P}(A)\hat{C}(C2);\\ &\vec{a} = [1 \quad 0 \quad 0 \quad 0]\,\hat{A};\\ &I_{\text{det}} = \vec{a}\hat{M}_S\vec{S}_{C1}. \end{aligned} \tag{1}$$

Here $\vec{S}_{\text{inc}}$ is the Stokes vector of light incoming from the synchrotron source into the PSG, $\vec{S}_{C1}$ is the Stokes vector incident on the sample, $\vec{S}_{C1}$ changes while sampling different values of P and $C1$, determining configuration of the PSG. $\hat{P}(P)$ and $\hat{P}(A)$ are Mueller matrices of a linear polarizer rotated at azimuths P and A, and $\hat{C}(C1)$, $\hat{C}(C2)$ are Mueller matrices of a retarder rotated at azimuths $C1$ and $C2$.[28] Vector $\vec{a}$ is the first row of the matrix $\hat{A}$, which changes with different configuration of the PSA, determined by the azimuths of the retarder $C2$ and the analyzer A.

To measure all 16 components of the sample Mueller matrix $\hat{M}_S$, at least 16 measurements of the I_{det} have to be taken with different configurations of the PSG and PSA. Typically I_{det} is measured for four different configurations of the PSG, each measured with four different PSA configurations, making 16 measurements altogether. Each of the $j = 1, \ldots, 4$ PSG configurations will provide incident light at the sample with Stokes vector $\vec{S}_{C1}{}^j$, and each of the $i = 1, \ldots, 4$ configurations of the PSA will be characterized by four vectors $\vec{a}^i$. If $\hat{I}$ is a matrix, containing detector intensities, measured with a combination of $\vec{a}^i$ and $\vec{S}_{C1}{}^j$, its elements are given by: $I_{ij} = \vec{a}^i \hat{M}_S \vec{S}_{C1}{}^j$. Similarly, we can define a 4×4 matrix $\hat{\sigma}$ with its jth column filled with $\vec{S}_{C1}{}^j$, and a 4×4 matrix $\hat{a}$, with rows filled by $\vec{a}^i$, and we can write the following equations:[29]

$$\begin{aligned} \hat{I} &= \hat{a}\hat{M}_S\hat{\sigma}; \\ \hat{M}_S &= \hat{a}^{-1}\hat{I}\hat{\sigma}^{-1}. \end{aligned} \tag{2}$$

Our software uses Eqs. (1) and (2) to calculate Mueller matrix of the sample from the measured intensities I_{ij} taking into account the selected PSG and PSA configurations $\{P,C1,C2,A\}$ and parameters of retarders obtained from the instrument calibration (see Fig. 5).

Provided an estimate of the Mueller matrix of the measured sample, the software also allows to estimate measurement uncertainties for a chosen set of sampled PSA and PSG states, based on the condition numbers of matrices $\hat{a}$ and $\hat{\sigma}$, and thus optimize the choice of PSA and PSG configurations involved in the measurement. In order for all components of sample Mueller matrix to be measureable, both matrices $\hat{\sigma}$ and $\hat{a}$ must have an inverse matrix, and thus must have ranks of at least four. This requires measurements with at least 4 different and independent states of PSA and 4 different and independent states of PSG. When there are more than 4 rows in the matrix $\hat{a}$ and matrix $\hat{\sigma}$ having more than 4 columns, the inverses, can be calculated as "pseudo-inverses" in the least-squared sense. It is also important, that both $\hat{a}$ and $\hat{\sigma}$ are well conditioned, so that the matrix inversion is stable, and does not amplify measurement errors.

Condition number of the matrix is defined as a ratio of the largest to the smallest eigenvalues magnitudes. When condition number of the matrix is infinite—matrix has at least one zero eigenvalue, is degenerate, and has no inverse. When condition number of the matrix is very large, matrix inversion becomes numerically less stable, and small uncertainties in measured intensities I_{ij} will result in large uncertainties in $\hat{M}_S = \hat{a}^{-1}\hat{I}\hat{\sigma}^{-1}$. Condition numbers closer to 1 make results of the matrix inversion more numerically stable, and less sensitive to the errors in the measured data, rounding errors, and other perturbations. Essentially, it is a measure of linear independence of the Stokes vectors generated by the PSG, and the Stokes states sampled by the PSA. When retarder in PSG ($C1$) is fixed, it turns out that matrix $\hat{\sigma}$ has zero determinant, no matter what the $C1$, or P values are, and therefore it is impossible to measure all 16 components of the sample Mueller matrix without rotating the retarder. The best condition value is realized when the four Stokes vectors produced by the PSG form a regular tetrahedron on the Poincare sphere.[30,31] Determinant of the condition matrix is related to the volume of such tetrahedron, and this configuration provided the largest volume possible. In this configuration the retarder should have retardation of 90°, both retarders and polarizers in the PSG (or PSA) have to rotate. Sabatke *et al.*[32] found that if the polarizer in the PSG or PSA has to be fixed due to some design considerations, the best condition value is achieved with the retardation of the retarders to be about 132°. Indeed, in our ellipsometer the 132° design of the rotating retarders and stationary linear polarizers would be advantageous due to the linear polarization of the synchrotron source and an automatic exclusion of the measurement errors due to polarization sensitivity of detectors. Nevertheless, we still keep the more traditional "close to 90° retardation" design of the retarders and implement the full range of rotation for all polarizers and retarders in PSG and in PSA. It allows us to use the same optics for transmission polarimetry experiments in magnetic field that is also implemented at our U4-IR beamline at NSLS-BNL. Our simulation software enables modeling the whole experimental setup, thus providing users with the opportunity to select the optimal measurement schedule, sampling PSG and PSA states, optimizing the condition numbers for PSG and PSA matrices, as well as optimizing detector intensity accounting for the losses in the retarders, and elsewhere along the optical path. Data analysis relies on the independent calibrations of the retarders and polarizers of the PSA and PSG.

V. BASICS OF THE RAE AND MM-SE TECHNIQUES

Spectroscopic ellipsometry (SE) analyses changes of the light polarization upon reflection from a sample in a wide range of electromagnetic spectrum. This technique has several methodological realizations, such as the previously mentioned RAE and MM-SE, and also rotating compensator ellipsometry (RCE), transmission polarimetry, and generalized ellipsometry (GE). Multiple books and reviews describe ellipsometry in great details.[33–40] In this section, we will summarize and explain only the basic concepts of RAE and MM-SE that are essential for understanding of the new instrument design and operations.

In conventional realization of RAE, polarization of reflected light is measured at an oblique AOI using a rotating linear polarizer. The complex Fresnel coefficients r_s and r_p for s- and p-polarized light are related to the so-called *pseudo* dielectric function of the sample as follows:

$$\tilde{\varepsilon} = \sin^2\theta + \sin^2\theta \cdot \tan^2\theta \cdot \left[\frac{1-\rho}{1+\rho}\right]^2, \tag{3}$$

where ρ is a ratio of Fresnel coefficients $\rho = r_p/r_s = \tan\Psi \cdot e^{i\Delta}$, $\tan\Psi = |r_p/r_s|$ is the ratio of reflection amplitudes, $\Delta = \delta_p - \delta_s$ is the phase difference between s- and p-polarized light, and θ is the AOI. The main advantage of spectroscopic ellipsometry is an unambiguous mathematical transformation between $\Psi(\omega)$ and $\Delta(\omega)$ and the real and imaginary parts of $\tilde{\varepsilon}(\omega)$ [Eq. (3)]. The true art of RAE is in a correct compensation for experimental errors, such as in the case of completely transparent or strongly metallic samples with $\sin(\Delta(\omega)) \approx 0$, and in the conversion from the measured pseudo dielectric

function to the true values of $\hat{\varepsilon}'(\omega)$ and $\hat{\varepsilon}''(\omega)$ for each layer of thin films and multilayer samples.

In spite of a broad range of RAE applications for isotropic bulk and thin-film samples with magnetic permeability $\mu(\omega) = 1$, where the $\{\Psi,\Delta\}$ formalism is sufficient for all practical needs, RAE has serious limitations for anisotropic and bi-anisotropic samples, i.e., when the p and s polarization states are not the eigenpolarizations of reflection. In these cases, the complete representation of reflection can be obtained only with addition of the off-diagonal components $\{r_{sp}, r_{ps}\}$ of the sample's Jones matrix $\hat{r} = \begin{bmatrix} r_{ss} & r_{sp} \\ r_{ps} & r_{pp} \end{bmatrix}$ measured at multiple AOIs and the sample azimuthal angles.[41] Thus, for anisotropic and/or magnetically ordered samples, ME materials, and samples with chirality, the RAE approach [Eq. (3)] is usually replaced or complemented with GE or MM-SE.[42–47] The MM formalism is based on the Stokes vector representation for the light polarization,[40] where the real components of the Stokes vectors for the input $\vec{S}_{IN}$ and output $\vec{S}_{OUT}$ light are connected with the 4 × 4 Muller matrix $\hat{M}$ of the sample as follows:

$$\vec{S}_{OUT} = \hat{M} \cdot \vec{S}_{IN}. \tag{4}$$

The 16 components of $\hat{M}$ are functions of the complex Fresnel coefficients[48]

$$\widehat{M} = \begin{pmatrix} \frac{1}{2}(|r_{pp}|^2 + |r_{ss}|^2 + |r_{sp}|^2 + |r_{ps}|^2) & \frac{1}{2}(|r_{pp}|^2 - |r_{ss}|^2 - |r_{sp}|^2 + |r_{ps}|^2) & \Re(r_{pp}r_{sp}^* + r_{ss}^* r_{ps}) & \Im(r_{pp}r_{sp}^* + r_{ss}^* r_{ps}) \\ \frac{1}{2}(|r_{pp}|^2 - |r_{ss}|^2 + |r_{sp}|^2 - |r_{ps}|^2) & \frac{1}{2}(|r_{pp}|^2 + |r_{ss}|^2 - |r_{sp}|^2 - |r_{ps}|^2) & \Re(r_{pp}r_{sp}^* - r_{ss}^* r_{ps}) & \Im(r_{pp}r_{sp}^* - r_{ss}^* r_{ps}) \\ \Re(r_{pp}r_{ps}^* + r_{ss}^* r_{sp}) & \Re(r_{pp}r_{ps}^* - r_{ss}^* r_{sp}) & \Re(r_{pp}r_{ss}^* + r_{ps}^* r_{sp}) & \Im(r_{pp}r_{ss}^* - r_{ps}^* r_{sp}) \\ -\Im(r_{pp}r_{ps}^* + r_{ss}^* r_{sp}) & -\Im(r_{pp}r_{ps}^* - r_{ss}^* r_{sp}) & -\Im(r_{pp}r_{ss}^* + r_{ps}^* r_{sp}) & \Re(r_{pp}r_{ss}^* - r_{ps}^* r_{sp}) \end{pmatrix}, \tag{5}$$

where $\Re$ and $\Im$ are the real and imaginary part operators. More details on conversion between complex 2 × 2 Jones and real 4 × 4 MM's, $r_{s,p,sp,ps} \Rightarrow M_{ij}$, can be found in Ref. 48. To compensate for both, the spectral variation of the incoming radiation and for the spectral response of the experimental setup, the MM components $M_{ij}(\omega)$ are usually replaced by the normalized ones $m_{ij}(\omega)$, where $m_{ij} = M_{ij}/M_{11}$. Note that in the reflection configuration M_{11} has a meaning of the total reflectivity of the sample. Thus, MM-SE can generate 15 normalized components of the MM, $\hat{m}$, which contain significantly more information about anisotropic, magnetic, and ME samples compared to that for $\Psi(\omega)$ and $\Delta(\omega)$ in Eq. (3). The theory of operations for MM-SE ellipsometry includes the following major steps:[41]

1. Polarization measurements of the MM components $M_{ij}(\omega, \theta)$ at several AOIs and correction for the systematic errors of experiment, such as non-ideal polarizers, retarders, windows, etc.
2. Sample modeling using, for example, a parametric description for the dielectric $\hat{\varepsilon}(\omega)$, magnetic $\hat{\mu}(\omega)$, and ME $\hat{\alpha}(\omega)$ and $\hat{\alpha}'(\omega)$ tensors and application of electromagnetic theory to calculate the MM spectra $M_{ij}(\omega, \theta)$, or solving a "direct problem": $\{\hat{\varepsilon}(\omega), \hat{\mu}(\omega), \hat{\alpha}(\omega), \hat{\alpha}'(\omega), \theta\} \Rightarrow M_{ij}(\omega, \theta)$.
3. Solving the "inverse problem" to determine the model input parameters, such as a number of the oscillator frequencies ω_0, and the correspondent broadening γ, and strength of electric and magnetic dipoles $S_{e,m}$, that provide the best match between experimental and modeled spectra: $M_{ij}(\omega, \theta) \Rightarrow \{\omega_0, S_{e,m}, \gamma, ...\}$.

VI. SIMULATIONS AND MEASUREMENTS FOR MAGNETIC AND ME MEDIA

A. Basics of the Berreman's 4 × 4 matrix formalism

Simulations of the optical properties of ME materials require solutions to Maxwell's equations. These solutions, in turn, depend upon the choice of the dielectric, magnetic, and ME models, which define the medium's constitutive relations:

$$\begin{aligned} \vec{D} &= \hat{\varepsilon}\vec{E} + \hat{\alpha}\vec{H} \\ \vec{B} &= \hat{\alpha}'\vec{E} + \hat{\mu}\vec{H}. \end{aligned} \tag{6}$$

In Eq. (6), $\vec{D}$ is the dielectric displacement, $\vec{B}$ is the magnetic induction, $\vec{E}$ is the primary electric field vector, $\vec{H}$ is the primary magnetic field vector, $\hat{\varepsilon}$ is the dielectric permittivity tensor, $\hat{\mu}$ is the magnetic permeability tensor, and $\hat{\alpha}$ and $\hat{\alpha}'$ are the ME tensors.[49] Each tensor can be described by a 3 × 3 matrix.[50] Both tensors $\hat{\alpha}$ and $\hat{\alpha}'$ are complex and can have both real and imaginary parts. Energy conservation requires the following inequality: $\alpha' \cdot \alpha \leq \mu \cdot \varepsilon$, which is well known for the static case of $\omega = 0$. Using numerical simulations, we found that this inequality should be also fulfilled for optical frequencies $\omega \neq 0$ in isotropic samples. In the case of anisotropic samples, analysis of this inequality is more complicated due to the nature of the complex tensors $\hat{\varepsilon}$, $\hat{\mu}$, $\hat{\alpha}$, and $\hat{\alpha}'$.[55] In general case, the upper limit for the values of $\hat{\alpha}$ and $\hat{\alpha}'$ in anisotropic medium is determined by the requirement that the z-component of the k-vector of light inside the medium should be $\mathrm{Re}(k_z) \geq 0$. In the case of a relatively high material symmetry, such as considered below in Sec. VI C, with nearly isotropic $\hat{\varepsilon}(\omega)$, $\hat{\mu}(\omega)$, and only one non-zero component of the ME tensors $\alpha_{xy}(\omega)$, our numerical

simulations show that the requirement of $\mathrm{Re}(k_z) \geq 0$ is equivalent to $\alpha'_{yx}(\omega) \cdot \alpha_{xy}(\omega) \leq \mu_{xx \approx yy}(\omega) \cdot \varepsilon_{xx \approx yy}(\omega)$. Based on the thermodynamic stability argument, Dzyaloshinskii suggested that $\hat{\alpha}' = \hat{\alpha}^T$ in the static case $\omega \to 0$.[51] This requirement for optical spectra when $\omega \neq 0$ is still under debate in the literature.[52] Thus, in the following discussion, we will keep a general notation for the $\hat{\alpha}$ and $\hat{\alpha}'$ tensors. In any case, both $\hat{\alpha}$ and $\hat{\alpha}'$ should have the same positive sign of their imaginary parts, so that the ME materials absorb radiation. Tensors $\hat{\alpha}$ and $\hat{\alpha}'$ change sign under space inversion and time inversion operations, remaining unchanged if both operations are applied simultaneously. This property results in the requirement that $\hat{\alpha} = \hat{\alpha}' \equiv 0$ in materials with the center of inversion or with time-reversal symmetry (see Refs. 53–55 for more detail). In this paper, we consider only ME effects. More general description of bi-anisotropic effects related to chirality can be found in Refs. 55–59.

The 4×4 matrix formalism, as developed by Berreman,[60] provides for an accurate and systematic method of obtaining numerical, and in some cases, analytic solutions for electromagnetic wave propagation in anisotropic, magnetic, ME, and bi-anisotropic materials. A complete description of electromagnetic wave propagation is made possible using Berreman's matrix equation:[28,60]

$$\begin{pmatrix} 0 & -curl \\ curl & 0 \end{pmatrix} \begin{pmatrix} \vec{E} \\ \vec{H} \end{pmatrix} = i\frac{\omega}{c} \begin{pmatrix} \hat{\varepsilon} & \hat{\alpha} \\ \hat{\alpha}' & \hat{\mu} \end{pmatrix} \begin{pmatrix} \vec{E} \\ \vec{H} \end{pmatrix}. \quad (7)$$

The 6×6 optical matrix in the right hand side of Eq. (7) contains $\hat{\varepsilon}(\omega)$, $\hat{\mu}(\omega)$, $\hat{\alpha}(\omega)$, and $\hat{\alpha}'(\omega)$, which completely describes the optical properties of, for example, ME materials.[28,60] Equation (7) can be reduced to the Berreman equation, which describes electromagnetic wave propagation in a crystal:

$$\frac{d\vec{\Psi}}{dz} = i\frac{\omega}{c}\tilde{\Delta}\vec{\Psi}, \quad (8)$$

$\vec{\Psi}$ is an array of the transverse components of the electromagnetic wave $\vec{\Psi} = [E_x, H_y, E_y, -H_x]^T$ in the medium and is an eigenvector of $\tilde{\Delta}$, where $\tilde{\Delta}$ is a 4×4 matrix constructed from the same set of components of the $\hat{\varepsilon}$, $\hat{\mu}$, $\hat{\alpha}$, and $\hat{\alpha}'$ tensors as the 6×6 optical matrix in Eq. (7). Note that $\vec{\Psi}$ and $\tilde{\Delta}$ in Eq. (8) have no relevance to the RAE variables $\Psi(\omega)$ and $\Delta(\omega)$.[61] The eigenvalues and eigenvector solutions to Eq. (8) represent wave vectors and the transverse components of the propagating electromagnetic waves, respectively. These solutions are unique to the crystal symmetries and constitutive relations incorporated into the $\tilde{\Delta}$ matrix.

The solution to the direct problem using the 4×4 matrix formalism follows the flowchart outlined in Fig. 6. This procedure begins with the 6×6 optical matrix, which enables the $\tilde{\Delta}$ matrix to be calculated along with its eigenvalues and eigenvectors. From the eigenvalues, the $\vec{k}$ vectors can be immediately determined which, in turn, allow for the analysis of possible birefringence in the medium. The eigenvectors, together with the tangential boundary conditions on $\vec{E}$ and $\vec{H}$ for incident media, provide for the solution of the complex reflection coefficients $r_{s,p,sp,ps}$. Finally, when the z components

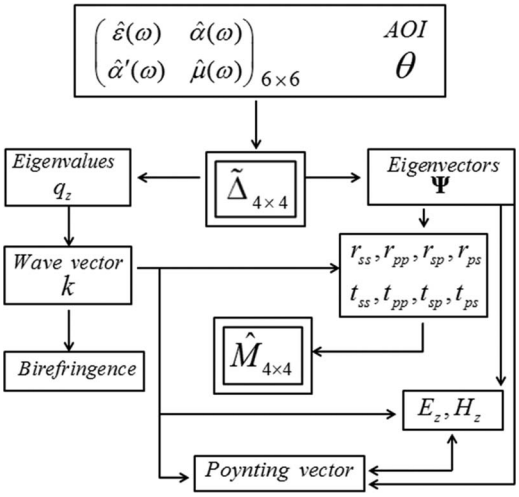

FIG. 6. Flowchart for the calculation steps in the 4×4 matrix formalism.

of $\vec{E}$ and $\vec{H}$ are recovered, the Poynting vector is returned, which can then be compared to the wave vector for analysis of possible divergence between the direction of the wave fronts and energy flow.

Various combinations of the tensors contained in Eqs. (6) and (7), and their allowed symmetries have been studied in the literature for bulk materials and thin films.[55,62] Many high-symmetry scenarios allow for analytical solutions for the Fresnel coefficients, and, hence, for the MM components. In this paper we will use the results of our numerical and analytical simulations that are based on the Berreman's 4×4 formalism to illustrate the applicability of the MM-SE to the studies of magnetic and ME materials. Note that the simplest case of a non-magnetic material with $\hat{\mu}(\omega) = 1$, and $\hat{\alpha}(\omega) = \hat{\alpha}'(\omega) = 0$ is well described in the literature and will not be considered in this paper.[44]

The modeling procedure for the optical properties of magnetic and ME materials begins with the symmetry consideration. In most material systems, this step allows to reduce the number of non-zero components in the $\hat{\varepsilon}$, $\hat{\mu}$, $\hat{\alpha}$, and $\hat{\alpha}'$ tensors below 15, which is the number of the normalized MM components measured for a single AOI. If no symmetry arguments are used, then the total number of $\hat{\varepsilon}$, $\hat{\mu}$, $\hat{\alpha}$, and $\hat{\alpha}'$ tensor components would correspond to about 36 complex functions of frequency, which may exceed several times the number of measured MM spectra for a single value of AOI making decoupling of the $\hat{\varepsilon}$, $\hat{\mu}$, $\hat{\alpha}$ and $\hat{\alpha}'$ tensor components practically impossible. Thus the symmetry consideration is equally important for both, numerical and analytical approaches to calculate the correspondent MM components. The complete correspondence table between the magnetic point symmetry groups and the symmetry of the $\hat{\varepsilon}$, $\hat{\mu}$, and $\hat{\alpha}$ tensors can be found in Ref. 63.

B. Magnetic materials with $\mu(\omega) \neq 1$, and $\alpha(\omega) = \alpha'(\omega) = 0$

In the presence of the center of inversion $\bar{1}$ or time-reverse invariance $1'$, which in most cases is equivalent to the absence of the macroscopic electrical polarization and/or

magnetization, the ME effect is forbidden by symmetry $\hat{\alpha}(\omega) = \hat{\alpha}'(\omega) = 0$. In the case of orthorhombic symmetry or higher, both $\hat{\varepsilon}$, and $\hat{\mu}$ tensors can become diagonal in the coordinate system that coincides with the major crystallographic and/or magnetic axes. In the ellipsometry convention, x direction is in the plane of the sample and along the reflection plane, y is in the sample plane and perpendicular to the reflection plane, and z is perpendicular to the sample surface. For example, if the a, b, and c directions of an orthorhombic crystal coincide with the measurement coordinates $x - y - z$, then the symmetric $\hat{\varepsilon}$ tensor has only three non-zero diagonal components: ε_{xx}, ε_{yy}, and ε_{zz}. The same argument about possible diagonalization is applicable to the symmetric $\hat{\mu}$ tensors. Note, however, that the primary axes of the $\hat{\mu}$ tensor are defined by the magnetic point group, which may or may not allow diagonalization in the same coordinates as the $\hat{\varepsilon}$ tensor. Among 3D point groups, only 32 non-magnetic and additional 90 magnetic groups are compatible with the crystal translation symmetry. Among 64 non-ME point groups (32 non-magnetic + 32 magnetic), only 8 groups do not permit simultaneous diagonalization of the $\hat{\varepsilon}$ and $\hat{\mu}$ tensors. Among them are the lowest-symmetry ones, such as, for example, $2'_z/m'_z$, and $2'_z/m'_z$, and $2_z/m_z$. The other 56 non-ME groups are generally relevant to the case considered below, such as, for example, A-type and G-type antiferromagnetic crystals with one of the A_x, A_y, A_z, G_x, G_y, or G_z spin order.

In Ref. 2 we calculated the Fresnel coefficients and MM components, which are applicable to both, metamaterials and natural magnetic materials and thin films with $\hat{\mu}(\omega) \neq 1$, and $\hat{\alpha}(\omega) = \hat{\alpha}'(\omega) = 0$. This case has analytical solutions if magnetic and dielectric tensors can be simultaneously diagonalized, thus reducing the number of independent non-zero components of the $\tilde{\Delta}$ matrix to ε_{xx}, ε_{yy}, ε_{zz}, μ_{xx}, μ_{yy}, μ_{zz}. Analysis of the MM components measured in reflection configuration shows that the contributions from the magnetic $\hat{\mu}(\omega)$ and dielectric $\hat{\varepsilon}(\omega)$ tensors have different sign in, for example, $M_{34}(\omega) = -M_{43}(\omega)$ components of the MM. Thus, if the frequencies of magnetic and electric dipole excitations are well separated, these excitations can be experimentally distinguished from each other without any additional modeling arguments.

An experimental example of ferrimagnetic Dy-iron garnet (Dy-IG) crystals, $Dy_3Fe_5O_{12}$, with a space group $Ia3d(O_h^{10})$ will be used below to illustrate a distinct behavior of electric and magnetic dipole modes in the MM spectra. Dy-IG has a cubic structure with a center of inversion and does not have any macroscopic electric polarization at room temperature.[64–66] Dy^{3+} ions with the ground state $^6H_{15/2}$ are in the 24d dodecahedral sites with the local orthorhombic symmetry 222(D_2). There are several non-equivalent Dy^{3+} ions in each unit cell with the same surrounding field, but the axes are inclined to each other. This has the overall effect of producing an average cubic symmetry. In spite of some recent indications of the local antiferroelectric ordering in both Dy-IG and in a related Tb-IG at low temperatures ($T < 100$ K),[67] these materials are not expected to have any observable ME effect in the optical spectra. The far-IR properties of Dy-IG, such as the frequencies of the optical phonons and magnons, are well-known from the previous optical transmission and reflection experiments.[4,68–71]

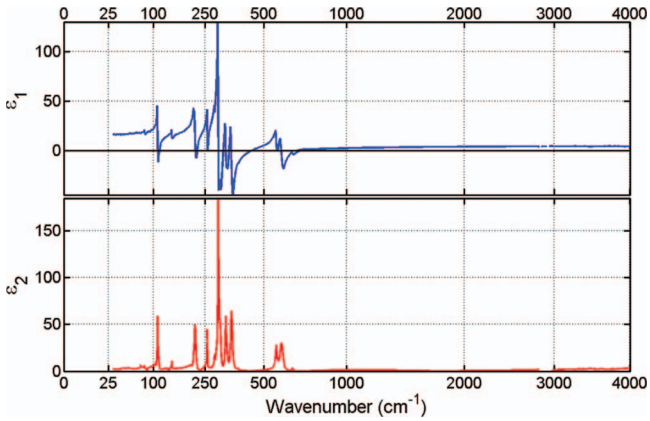

FIG. 7. Experimental RAE data for the real ε_1 and imaginary ε_2 parts of the dielectric function for Dy-IG measured at $T = 7$ K at AOI = 75° using three sets of detectors and two sets of the spectrometer beamsplitters. Strong peaks between 80 and 700 cm^{-1} are optical phonons.

Figure 7 shows broad range RAE spectra of Dy-IG measured between 30 and 4000 cm^{-1} at AOI = 75° and $T = 7$ K. These spectra have been obtained using three sets of linear polarizers and three types of detectors: LHe-pumped (1.6 K) bolometer, LHe (4.2 K) bolometer, and CuGe detector. The low-frequency cutoff is determined by the diffraction limit due to the size of the available crystal of about 5 × 5 mm^2. The strong peaks in the pseudo-dielectric function $\varepsilon_1(\omega)$ and $\varepsilon_2(\omega)$ between 80 and 700 cm^{-1} are optical phonons. Since the structural symmetry of garnets is close to cubic, so the pseudo-dielectric function in the optical phonon frequency range should coincide with the isotropic dielectric function except for the contribution of the magnetic modes. The $\hat{\varepsilon}(\omega)$ and $\hat{\mu}(\omega)$ tensors in the case of Dy-IG can be reduced down to the scalar functions and can be described using a combination of Lorentzian, or simple harmonic oscillators (SHO):

$$\varepsilon(\omega) = \varepsilon_\infty + \sum_{j=1}^{N} \frac{S_{j,e}{\omega_{j,e0}}^2}{\left({\omega_{j,e0}}^2 - \omega^2 - i\gamma_{j,e}\omega\right)},$$
$$\mu(\omega) = \mu_\infty + \sum_{j=1}^{M} \frac{S_{j,m}{\omega_{j,m0}}^2}{\left({\omega_{j,m0}}^2 - \omega^2 - i\gamma_{j,m}\omega\right)}, \quad (9)$$

where ε_∞ and μ_∞ are the infinite-frequency values of the dielectric function ($\mu_\infty \cong 1$), $S_{e,m}$ is the oscillator strength, $\gamma_{e,m}$ is the damping constant, and $\omega_{e0,m0}$ is the resonance frequency of the excitations, such as phonons and magnons.

Figure 8(a) shows normalized MM spectra, $m_{34} = -m_{43}$ and $m_{33} = m_{44}$ for the same Dy-IG crystal as in Fig. 7 measured using rotating Si retarders and stationary linear polarizers in the frequency range between 50 and 460 cm^{-1}. To simulate and fit the MM spectra we use our home-made program based on the Berreman's 4 × 4 formalism. The results of the simultaneous fit to the normalized MM spectra are shown in Fig. 8(a) with solid red curves. The two measurements, MM and RAE in Figs. 7 and 8, agrees within 10% for the oscillator strengths and practically coincide for the frequencies and broadening of the optical phonons.

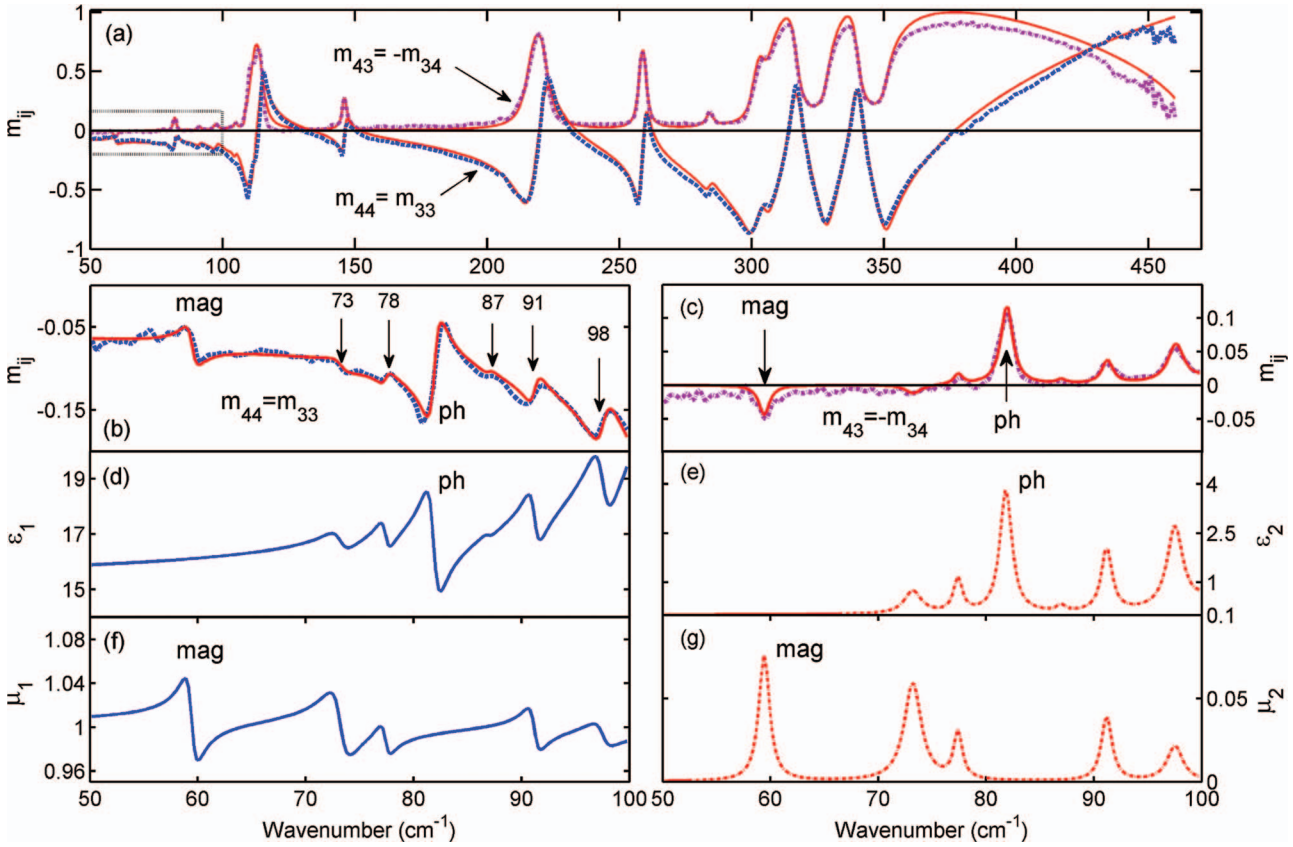

FIG. 8. (a) Experimental spectra of the normalized MM components $m_{34}(\omega) = -m_{43}(\omega)$ (magenta dotted-dashed curve) and $m_{33}(\omega) = m_{44}(\omega)$ (blue dashed curve) for Dy-IG measured at $T = 5$ K. The strong peaks above 80 cm^{-1} correspond to the optical phonons. Solid red curves show the fit results. (b)-(c) The low-frequency part of the same spectra measured with a LHe-pumped 1.6 K bolometer. The corresponding range is shown in (a) with a black dotted rectangle. (d)-(g) $\varepsilon_{1,2}(\omega)$ and $\mu_{1,2}(\omega)$ functions as extracted from the fit of the MM spectra. The pure magnetic dipole excitation (magnon) is observed at 59.5 cm^{-1} and the pure electric dipole excitation (phonon) is observed at 81 cm^{-1}. The magnon amplitude in the $m_{34}(\omega) = -m_{43}(\omega)$ spectra in (c) has an opposite sign compared to that for the optical phonon. A number of hybrid modes that contribute to both $\varepsilon_{1,2}(\omega)$ and $\mu_{1,2}(\omega)$ in (d)-(g) correspond to the weak crystal-field transitions and are marked in (b) with vertical arrows.

Figures 8(b) and 8(c) show the magnified view of the low-frequency part of the normalized MM spectra measured with the same optical components and a LHe-pumped (1.6 K) bolometer. Figures 8(d)–8(g) show $\varepsilon_{1,2}(\omega)$ and $\mu_{1,2}(\omega)$ functions extracted from the fit of the MM spectra. The pure magnetic dipole excitation (magnon) appears at 59.5 cm^{-1}, which is exactly the same frequency as previously determined.[4,71] Pure electric dipole excitation at 81 cm^{-1} corresponds to the optical phonon. Our measurements demonstrate [see Fig. 8(c)] that the sign of the magnon contribution in $m_{34}(\omega) = -m_{43}(\omega)$ is negative, that is opposite to that for the electric dipoles, such as the phonon at 81 cm^{-1}. The spectra in Figs. 8(b) and 8(c) also show several weak ligand-field excitations at 73, 78, 87, 91, and 98 cm^{-1}, which originate from 4*f* electronic levels in Dy^{3+} ions. From Figs. 8(d)–8(g) one can see that these modes contribute to both $\varepsilon(\omega)$ and $\mu(\omega)$ and thus are hybrid (see Ref. 4 for more details on the hybrid modes). As expected for the material symmetry of Dy-IG, the measured off-diagonal components of the MM are equal to zero: $m_{13,31} = m_{14,41} = m_{23,32} = m_{24,42} \cong 0$ within the accuracy of our experiments. We did not detect any changes in the off-diagonal MM components if measured at temperatures below and above the antiferroelectric transition at $T \approx 100$ K.

C. Multiferroics and ME materials with $\mu(\omega) \neq 1$ and $\alpha(\omega) \neq 0$

Spectra of electromagnons in MF crystals $TbMnO_3$ and $GdMnO_3$ have been discovered by Pimenov *et al.*[72] This discovery was followed by a number of research groups and the emergence of electromagnons was discussed for a broad variety of magnetic oxides such as perovskite $RMnO_3$,[73–77] RMn_2O_5,[78] hexagonal $YMnO_3$,[79] $BiFeO_3$,[80,81] $Ba_2Mg_2Fe_{12}O_{22}$,[82,83] $CuFe_{1-x}Ga_xO_2$,[84] and $Ba_2CoGe_2O_7$.[85] The common feature for electromagnons in all those materials is the polarization selection-rules. The electromagnon mode is predominantly excited by an electric field of light, in contrast to the case of the magnons, or antiferromagnetic resonances, that can be excited by the magnetic field component of light only. However, the polarization analysis of the electromagnon spectra has been so far restricted by the experimental geometry with the normal light incidence on the sample surface. The limitations of this approach revealed themselves recently by failing to explain the experimentally observed suppression of electromagnons in reflectivity measurements of $GdMnO_3$.[86] As we will show in this section, MM-SE is capable to provide more information about the electromagnon spectra.

MF and ME materials, such as, for example, $TbMnO_3$ and $TbMn_2O_5$, are particularly interesting since in the low-temperature phases the symmetry allows both, the electric polarization and magnetic order. As a result, the ME tensor in the optical part of the spectrum may be nonzero at least in some components: $\alpha(\omega) \neq 0$ and $\alpha'(\omega) \neq 0$. Due to the requirement of $\alpha'(\omega) \cdot \alpha(\omega) \leq \mu(\omega) \cdot \varepsilon(\omega)$, we expect the strongest contribution in ME tensors at the frequencies where $\mu(\omega)$ and $\varepsilon(\omega)$ have poles, i.e., close to the resonances with phonons, magnons, and electromagnons. The requirement that $\alpha \neq 0$ infers a simultaneous absence of both center of inversion and the time-reverse invariance. In symmetry terms, the total number of magnetic point groups that allow ME effects is 58. The simulation analysis for the contributions of the $\hat{\varepsilon}$, $\hat{\mu}$, $\hat{\alpha}$, and $\hat{\alpha}'$ tensor components to the MM spectra shows that the $\hat{\varepsilon}$ and $\hat{\mu}$ should reveal themselves in the close-to-diagonal $m_{ij}(\omega)$, such as m_{12}, m_{21}, m_{33}, m_{44}, m_{34}, and m_{43}. In contrast, the appearance of non-zero $\hat{\alpha}$ and $\hat{\alpha}'$ tensors is equivalent to optical bi-anisotropy and should give some contribution to the m_{13}, m_{14}, m_{23}, m_{24}, m_{31}, m_{32}, m_{41}, and m_{42} spectra.

Optical spectra of $TbMnO_3$, measured using both optical transmission and reflectivity have been studied extensively in the last several years.[72,76,87] It was shown that the electric component of light directed along the a axis apart from excitation of optical phonons with frequencies above 100 cm^{-1}, can excite both electromagnons at 19 and 62 cm^{-1}, and another excitation at 135 cm^{-1}. The latter excitation at 135 cm^{-1} has a controversial interpretation in the literature and was assigned to two-magnon process, one-phonon+one-magnon process or transition between crystal-field levels of the Tb^{3+} ground multiplet. Figure 9 shows the low-frequency part of the RAE and MM spectra measured with LHe-pumped bolometer and Si retarders at AOI = 75°. All measurements in Fig. 9 were taken when the crystallographic directions of $TbMnO_3$ are oriented with respect to the ellipsometric axes $x - y - z$ as follows: $x \| a$, $y \| c$, and $z \| b$. The cross section of the available to us sample was only 5 × 5 mm^2, which resulted in the low-frequency cutoff at ~25 cm^{-1} thus preventing the measurement of the lowest frequency electromagnon mode at ~19 cm^{-1}. The pseudo-dielectric function $\langle \varepsilon_1 \rangle$ in Fig. 9(a), which was obtained from RAE spectra measured at different temperatures between 5 K and 38 K, shows a clear re-distribution of the spectral weight from the optical phonon at 118.5 cm^{-1} towards electromagnon at 62, and excitation at 135 cm^{-1} which we label as EX. The exchange of the spectral weight occurs below the transition temperature of $T_C = 28$ K. The shape of the electromagnon peak in RAE measurements is different from that of the phonons and cannot be easily described with a SHO model indicating the limitations of the pseudo-dielectric function approach to the optical spectra of ME materials. The normalized MM components of the same sample are shown in Figs. 9(b) and 9(c). The same peaks that correspond to the electromagnon, single phonon and EX are clearly seen in $m_{33} = m_{44}$ and $m_{34} = -m_{43}$ spectra at 62, 118.5, and 135 cm^{-1}. Note that the sign of the electromagnon contribution to the $m_{34} = -m_{43}$ spectra is the same as that for the phonon, thus proving unambiguously a well-known fact that the electromagnon excitation is indeed a predominantly electric dipole polarized along the a axis of $TbMnO_3$.

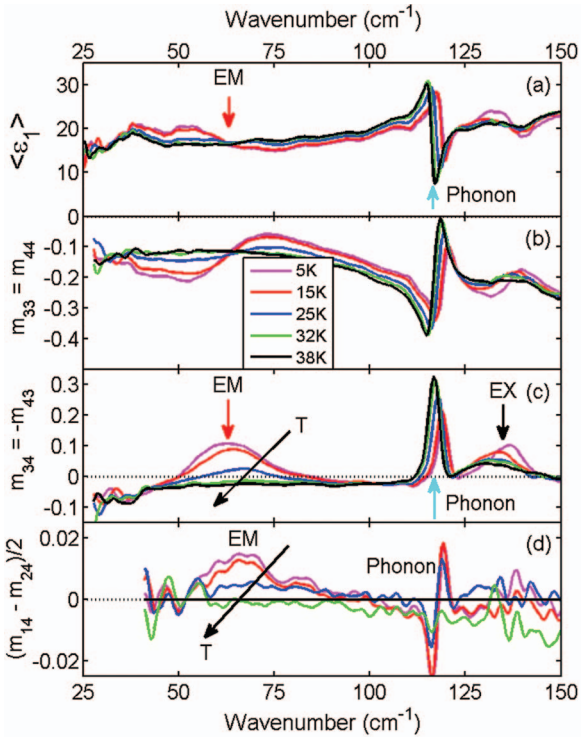

FIG. 9. Experimental optical spectra of $TbMnO_3$ with crystallographic orientation of $x \| a$, $y \| c$, and $z \| b$ measured in the temperature range between 5 K and 40 K. Phonon peak at ~118.5 cm^{-1}, electromagnon (EM) peak at 62 cm^{-1}, and peak of excitation at 135 cm^{-1} (EX) are marked with arrows. (a) Real part of the pseudo-dielectric function. The normalized MM components are shown in (b) $m_{34}(\omega) = -m_{43}(\omega)$ and (c) $m_{33}(\omega) = m_{44}(\omega)$. (d) The difference between the off-diagonal MM components $m_{14}(\omega)$ and $m_{24}(\omega)$. Vertical arrows in (c) indicate the contribution of $\varepsilon_{xx}(\omega)$, $\mu_{yy}(\omega)$, and $\alpha_{xy}(\omega)$ to $m_{34}(\omega) = -m_{43}(\omega)$ components of the MM spectra.

Figure 9(d) shows the difference between the normalized off-diagonal components of the MM, which are proportional to the electromagnon's contribution to the $\hat{\alpha}$ and $\hat{\alpha}'$ tensors. The symmetry consideration for the cycloidal spin structure in $TbMnO_3$ predicts that only $\alpha_{xz} \neq 0$.[52] It is this component of the $\hat{\alpha}$ tensor that provides the coupling between the dynamic polarization of the lattice along the a axis and magnetization caused by an external magnetic field applied along the b axis.[88] For $\alpha_{xz} \neq 0$, the electromagnon's contribution in m_{24} and m_{14} spectra has opposite sign. To exclude small offsets caused by the polarizer/retarder calibration errors, we plot the difference $(m_{24} - m_{14})/2$, which shows a pure contribution from electromagnon to the off-diagonal components of the MM. The low-temperature amplitude of the electromagnon peak in $(m_{24} - m_{14})/2$ is about 0.015, which is smaller than the contribution of the same electromagnon to $m_{34} = -m_{43}$ of about 0.1 The combined fit of the MM spectra resulted in the following parameters of electromagnon at $T = 5$ K: $\omega_0 = 62 \pm 2$ cm^{-1}, $\gamma_0 = 20 \pm 2$ cm^{-1}, $S_{e,xx} = 1.7 \pm 0.2$ and $S_{EM,xz} = 0.2 \pm 0.05$. The spectral variation of $\alpha_{xz}(\omega)$ was calculated with these parameters using SHO model,

$$\alpha_{xz}(\omega) = \sum_{j=1}^{N} \frac{S_{j,EM}\omega_{j,EM0}{}^2}{\left(\omega_{j,EM0}{}^2 - \omega^2 - i\gamma_{j,EM}\omega\right)}. \quad (10)$$

The oscillator strengths of electromagnon $S_{e,xx}$ and $S_{EM,xz}$ determined from the MM measurements are important parameters that are related to the electric polarization of the lattice due to the spin structure, and anisotropy and exchange fields.[52] The calculated maximum value of the ME function is $|\alpha_{xz}(\omega)| \leq 0.5$, which is ~10 times smaller than the theoretical limit of $\alpha(\omega)^{\max} = \sqrt{\mu(\omega) \cdot \varepsilon(\omega)} \approx 5$. An experimental verification of all symmetry properties of the ME tensors in $TbMnO_3$, such as the fact that the diagonal components of the $\hat{\alpha}$ tensor are indeed equal to zero and verifying that $\hat{\alpha}^T = \hat{\alpha}'$, would require additional measurements of same sample with other orientations of the *a*-*b*-*c* axes with respect to the *x*-*y*-*z* ellipsometer coordinate system. Details of the fit for the coupled electromagnon and phonon excitation at 62 cm^{-1} in the MM spectra measured at different AOIs and crystal orientations using hybrid oscillator model will be published elsewhere.

VII. CONCLUSIONS

A new far-IR ellipsometer with a full MM capability has been designed and installed at U4IR beamline at NSLS-BNL. There are several design features, which differentiate this instrument from other far-IR ellipsometers.

1. A broad spectral range of the instrument between 20 and 4000 cm^{-1} is facilitated by the properties of the SR, which we use as a light source at U4IR beamline, NSLS-BNL, and is provided by the use of the interchangeable sets of optical polarizers, retarders, spectrometer beamsplitters, and detectors. The high brightness of the synchrotron source, especially in the frequency range below 100 cm^{-1}, is crucial for the studies of relatively small crystals with an in-plane cross section area of a few mm^2.
2. The spot-size of about 3 × 3 mm^2 at the sample position for the slowly focused SR with $f_{\#} = 20$ is facilitated by the use of parabolic mirrors. Since the light source at U4IR is diffraction-limited in the spectral range below 1000 cm^{-1}, our ellipsometer provides a relatively small spot size of the focused radiation without intensity-reducing apertures.
3. Our setup is equipped with several sets of rotating retarders for a broad frequency range including the far-IR that enables a full Muller matrix analysis or the samples.
4. The experiments are supported by our recent developments in the theory of operations, data analysis, and data simulation/fitting for full-Muller-matrix measurements of dielectric and magnetic properties of complex materials and thin film structures. We apply 4 × 4 Berreman's matrix formalism to calculate complex reflection coefficients and the corresponding MM spectra in complex materials.
5. A mechanical stability and reproducibility of the measurements is provided by an integrated 2-circle goniometer assembly and an XYZ translation stage for the sample positioning. The whole instrument is controlled by a single LabVIEW program.

This ellipsometer setup will become a part of the planned MET beamline at the NSLS-II synchrotron light source, expected to be operational in 2015. Among the design improvements will be an optimized extraction and optical transport of SR to the ellipsometer in order to reduce diffraction losses at long wavelengths.

ACKNOWLEDGMENTS

The authors are thankful to Christian Bernhard, Adam Dubroka, Prema Marsik, Josef Humlíček, Alexander Boris, Stefan Zollner, Tino Hofmann, Mathias Schubert, and Andrew Van Dyke for useful discussion of the instrument design and operations. Many thanks to Sang W. Cheong and Andrey Maljuk for the samples. We appreciate the everyday support from Randy Smith, Gary Nintzel, Michael Caruso, Dennis Carlson, and Qing-Yi Dong at U4IR beamline, NSLS-BNL. We are thankful to Raymond Conley at BNL for help with the Si prism retarders. An invaluable help from the Rutgers Machine shop lead by William Schneider is greatly appreciated. The development of the instrument in 2008–2010 was supported by NSF under Grant No. DMR-0821224. The measurements at NJIT in 2010–2012 were supported by the U.S. Department of Energy under Grant No. DE-FG02-07ER46382. The National Synchrotron Light Source is operated as a User Facility for the U.S. Department of Energy under Contract No. DE-AC02-98CH10886.

APPENDIX A: GENERALIZED ELLIPSOMERY VS. MM-SE

Generalized ellipsomery is another closely related approach, which is based on the Jones matrix for anisotropic samples $\hat{J}$.[42–48] The components of the Jones matrix are usually normalized by r_{ss}:

$$\hat{J} = \begin{pmatrix} r_{pp} & r_{ps} \\ r_{sp} & r_{ss} \end{pmatrix} = r_{ss} \begin{pmatrix} r_{pp}/r_{ss} & r_{ps}/r_{ss} \\ r_{sp}/r_{ss} & 1 \end{pmatrix}, \quad \text{(A1)}$$

where $r_{pp}/r_{ss} = \tan\psi_{pp} \exp(i\Delta_{pp})$, $r_{ps}/r_{ss} = \tan\psi_{ps} \exp(i\Delta_{ps})$, and $r_{sp}/r_{ss} = \tan\psi_{sp} \exp(i\Delta_{sp})$. Accordingly, the complex Jones matrix of anisotropic samples is defined by six parameters only: $\tan\psi_{pp}$, $\tan\psi_{sp}$, $\tan\psi_{ps}$, Δ_{pp}, Δ_{sp}, and Δ_{ps}. Note, however, that a reduction of the number of independent parameter in GE compared to that in MM-SE does not necessarily result in a loss of information about the sample properties since both approaches utilize the same set of the Fresnel coefficients. It is a common belief that in the absence of depolarization both approaches are practically equivalent. A detailed comparison of GE and MM-SE can be found in Ref. 48.

APPENDIX B: COMPARISON OF SR-BASED AND THE THZ TIME-DOMAIN SPECTROSCOPIC ELLIPSOMETRY

Several research groups focused recently on development of the THz time-domain spectroscopic ellipsometry.[39,89–91] For example, Neshat and Armitage[91] described a new ellipsometers setup for the frequency range between 3 and

50 cm^{-1} with a variable AOI capability. To produce a THz radiation, this group is using a hollow core photonic band gap fiber with no pre-chirping in order to deliver a femtosecond laser into a THz photoconductive antenna. The obvious advantage of the THz-TDS approach is in application of an affordable table-top light source for the THz spectral range. Among limitations of this technique one can mention a narrow spectral range and the light focusing issues. Due to the fast focusing with $f_{\#} = 8$, as described in Ref. 91, the uncertainty in the incidence angle may result to necessity for heavy-math correction procedures for the measured ellipsometry data for anisotropic samples.

[1]W. S. Weiglhofer and A. Lakhtakia, *Introduction to Complex Mediums for Optics and Electromagnetics* (SPIE Optical Engineering, Bellingham, Washington, 2003).
[2]P. D. Rogers, T. D. Kang, T. Zhou, M. Kotelyanskii, and A. A. Sirenko, Thin Solid Films **519**, 2668 (2011).
[3]T. D. Kang, E. Standard, G. L. Carr, T. Zhou, M. Kotelyanskii, and A. A. Sirenko, Thin Solid Films **519**, 2698 (2011).
[4]P. D. Rogers, Y. J. Choi, E. C. Standard, T. D. Kang, K. H. Ahn, A. Dubroka, P. Marsik, Ch. Wang, C. Bernhard, S. Park, S.-W. Cheong, M. Kotelyanskii, and A. A. Sirenko, Phys. Rev. B **83**, 174407 (2011).
[5]T. N. Stanislavchuk, A. A. Sirenko, A. P. Litvinchuk, X. Luo, and S.-W. Cheong, J. Appl. Phys. **112**, 044108 (2012).
[6]D. W. Jeong, W. S. Choi, T. D. Kang, C. H. Sohn, A. David, H. Rotella, A. A. Sirenko, C. H. Lee, J. H. Kim, U. Lüders, W. Prellier, Y.-J. Kim, Y. S. Lee, and T. W. Noh, Phys. Rev. B **84**, 115132 (2011).
[7]J. Kircher, R. Henn, M. Cardona, P. L. Richards, and G. P. Williams, J. Opt. Soc. Am. B **14**, 705 (1997).
[8]R. Henn, C. Bernhard, A. Wittlin, M. Cardona, and S. Uchida, Thin Solid Films **313–314**, 642 (1998).
[9]C. Bernhard, R. Henn, A. Wittlin, M. Kläser, G. Müller-Vogt, C. T. Lin, and M. Cardona, Phys. Rev. Lett. **80**, 1762 (1998).
[10]A. A. Sirenko, C. Bernhard, A. Golnik, A. M. Clark, J. Hao, W. Si, and X. X. Xi, Nature (London) **404**, 373 (2000).
[11]C. Bernhard, D. Munzar, A. Wittlin, W. König, A. Golnik, C. T. Lin, M. Kläser, Th. Wolf, G. Müller-Vogt, and M. Cardona, Phys. Rev. B **59**, R6631 (1999).
[12]C. Bernhard, T. Holden, J. Humlicek, D. Munzar, M. Cardona, and B. Keimer, Solid State Commun. **121**, 93 (2002).
[13]A. V. Pimenov, A. V. Boris, Li Yu, V. Hinkov, Th. Wolf, B. Keimer, and C. Bernhard, Phys. Rev. Lett. **94**, 227003 (2005).
[14]C. Bernhard, A. V. Boris, N. N. Kovaleva, G. Khaliullin, A. Pimenov, D. P. Chen, C. T. Lin, and B. Keimer, Phys. Rev. Lett. **93**, 167003 (2004).
[15]N. N. Kovaleva, A. V. Boris, C. Bernhard, A. Kulakov, A. Pimenov, A. M. Balbashov, G. Khaliullin, and B. Keimer, Phys. Rev. Lett. **93**, 147204 (2004).
[16]A. V. Boris, N. N. Kovaleva, T. Holden, O. V. Dolgov, C. T. Lin, B. Keimer, and C. Bernhard, Science **304**, 708 (2004).
[17]A. V. Boris, Y. Matiks, E. Benckiser, A. Frano, P. Popovich, V. Hinkov, P. Wochner, M. Castro-Colin, E. Detemple, V. K. Malik, C. Bernhard, T. Prokscha, A. Suter, Z. Salman, E. Morenzoni, G. Cristiani, H.-U. Habermeier, and B. Keimer, Science **332**, 937 (2011).
[18]S. S. A. Seo, W. S. Choi, H. N. Lee, L. Yu, K. W. Kim, C. Bernhard, and T. W. Noh, Phys. Rev. Lett. **99**, 266801 (2007).
[19]A. Dubroka, M. Rössle, K. W. Kim, V. K. Malik, L. Schulz, S. Thiel, C. W. Schneider, J. Mannhart, G. Herranz, O. Copie, M. Bibes, A. Barthélémy and C. Bernhard, Phys. Rev. Lett. **104**, 156807 (2010).
[20]Li Yu, D. Munzar, A. V. Boris, P. Yordanov, J. Chaloupka, Th. Wolf, C. T. Lin, B. Keimer, and C. Bernhard, Phys. Rev. Lett. **100**, 177004 (2008).
[21]A. Charnukha, P. Popovich, Y. Matiks, D. L. Sun, C. T. Lin, A. N. Yaresko, B. Keimer, and A. V. Boris, Nat. Commun. **2**, 219 (2011).
[22]C. Bernhard, J. Humlıcek, and B. Keimer, Thin Solid Films **455–456**, 143 (2004).
[23]A. Röseler, U. Schade, and K. Hoildack, in *the Proceedings of the joint 30th International Conference on Infrared and Millimeter Waves and 13th International Conference on Terahertz Electronics, Williamsburg, VA, 2005*, edited by K. J. Button and G. R. Neil (IEEE, Piscataway, NJ, 2005), Vol. 1, p. 190.
[24]W. J. Padilla, Z. Q. Li, K. S. Burch, Y. S. Lee, K. J. Mikolaitis, and D. N. Basov, Rev. Sci. Instrum. **75**, 4710 (2004).
[25]D. T. Chuss, S. H. Moseley, G. Novak, and E. J. Wollack, Proc. SPIE **5492**, 1487 (2004).
[26]T. Hofmann, U. Schade, W. Eberhardt, C. M. Herzinger, P. Esquinazi, and M. Schubert, Rev. Sci. Instrum. **77**, 063902 (2006).
[27]C. J. Hirschmugl and G. P. Williams, "Infrared synchrotron radiation: Programs at the NSLS," Synchrotron Radiat. News **8**, 10 (1995).
[28]R. M. A. Azzam and N. M. Bashara, *Ellipsometry and Polarized Light* (North-Holland, Amsterdam, 1977).
[29]A. DeMartino, E. Garcia-Caurel, B. Laude, and B. Drevillon, Thin Solid Films **455–456**, 112 (2004).
[30]A. Ambirajan and D. C. Look, Opt. Eng. **34**, 1651 (1995).
[31]A. Ambirajan and D. C. Look, Opt. Eng. **34**, 1656 (1995).
[32]D. S. Sabatke, M. R. Decour, E. L. Dereniak, W. C. Sweatt, S. A. Kemme, and G. S. Phipps, Opt. Lett. **25**, 802 (2000).
[33]D. E. Aspnes, in *Handbook of Optical Constants of Solids*, edited by E. D. Palik (Academic, New York, 1985), p. 89.
[34]M. Schubert, in *Handbook of Ellipsometry*, edited by G. Irene and H. Tompkins (William Andrew, Norwich, NY, 2005), p. 637.
[35]G. E. Jellison, Jr., Thin Solid Films **313–314**, 33 (1998).
[36]U. Rossow and W. Richter, in *Optical Characterization of Epitaxial Semiconductor Layers*, edited by G. Bauer and W. Richter (Springer, New York, 1996), p. 68.
[37]H. Fujiwara, *Spectroscopic Ellipsometry: Principles and Applications* (Wiley, 2007).
[38]T. Hofmann, U. Schade, C. M. Herzinger, P. Esquinazi, and M. Schubert, Proc. SPIE **6120**, 61200D (2006).
[39]T. Hofmann, C. M. Herzinger, A. Boosalis, T. E. Tiwald, J. A. Woollam, and M. Schubert, Rev. Sci. Instrum. **81**, 023101 (2010).
[40]A. Röseler, *Infrared Spectroscopic Ellipsometry* (Akademie, Berlin, 1992).
[41]R. M. A. Azzam, *Handbook of Optics*, edited by M. Bass *et al.* (McGraw-Hill, New York, 1995), Vol. II, Chap. 27.
[42]M. Schubert, B. Rheinländer, B. Johs, C. M. Herzinger, and J. A. Woollam, J. Opt. Soc. Am. A **13**, 875 (1996).
[43]M. Schubert, T. E. Tiwald, and J. A. Woollam, Appl. Opt. **38**, 177 (1999).
[44]M. Schubert, Phys. Rev. B **53**, 4265 (1996).
[45]T. E. Tiwald and M. Schubert, Proc. SPIE **4103**, 19 (2000).
[46]M. Schubert, "Another century of ellipsometry," Ann. Phys. **15**, 480–497 (2006).
[47]M. Schubert, A. Kasic, T. Hofmann, V. Gottschalch, J. Off, F. Scholz, E. Schubert, H. Neumann, I. Hodgkinson, M. Arnold, W. Dollase, and C. M. Herzinger, "Generalized ellipsometry of complex mediums in layered systems," Proc. SPIE **4806**, 264 (2002).
[48]M. Schubert, T. Hofmann, and C. M. Herzinger, J. Opt. Soc. Am. A **20**(2), 347 (2003).
[49]I. V. Lindell, A. H. Sihvola, S. A. Tretyakov and A. J. Viitanen, *Electromagnetic Waves in Chiral and Bi-Isotropic Media* (Artech House, Boston, 1994).
[50]J. F. Nye, *Physical Properties of Crystals - Their Representation by Tensors and Matrices* (Oxford University Press, Oxford, 2006).
[51]I. E. Dzyaloshinskii, Sov. Phys. JETP **10**, 628 (1959).
[52]A. Cano, Phys. Rev. B **80**(18), 180416 (2009).
[53]T. H. O'Dell, *The Electrodynamics of Magneto-Electric Media* (North-Holland, Amsterdam, 1970).
[54]J.-P. Rivera, Eur. Phys. J. B **71**(3), 299 (2009).
[55]P. D. Rogers, M. Kotelyanskii, and A. A. Sirenko, e-print arXiv:1105.4934 [physics.optics].
[56]E. Georgieva, J. Opt. Soc. Am. A **12**, 2203 (1995).
[57]O. Arteaga, Opt. Lett. **35**, 1359 (2010).
[58]E. Bahar, J. Opt. Soc. Am. B **26**, 364 (2009).
[59]E. M. Georgieva, I. J. Lalov, and M. Gospodinov, Optik (Jena) **109**, 173–176 (1998).
[60]D. W. Berreman, J. Opt. Soc. Am. **62**, 502 (1972).
[61]In this paper we use here a similar notation for $\mathbf{\Psi}$, $\tilde{\Delta}$, $\Psi(\omega)$, and $\Delta(\omega)$ to be consistent with literature on both, Berreman's formalism and RAE.
[62]Q. Cheng and T. J. Cui, J. Opt. Soc. Am. A **23**, 3203 (2006).
[63]D. B. Litvin, "Property tensor invariant under magnetic point group," private communication, Penn State University, 2011.
[64]F. Sayetat, J. Magn. Magn. Mater. **58**, 334 (1986).
[65]F. Sayetat, J. X. Boucherle, and F. Tcheou, J. Magn. Magn. Mater. **46**, 219 (1984).

[66]R. Hock, H. Fuess, T. Vogt, and M. Bonnet, J. Solid State Chem. **84**, 39 (1990).
[67]D. Louca, K. Kamazawa, and T. Proffen, Phys. Rev. B **80**, 214406 (2009).
[68]A. J. Sievers and M. Tinkham, Phys. Rev. **129**, 1995 (1963).
[69]M. Tinkham, Phys. Rev. **124**, 311 (1961).
[70]J. Yamamoto, B. T. Smith, and E. E. Bell, J. Opt. Soc. Am. **64**, 880 (1974).
[71]T. D. Kang, E. C. Standard, P. D. Rogers, K. H. Ahn, A. A. Sirenko, A. Dubroka, C. Bernhard, S. Park, Y. J. Choi, and S.-W. Cheong, Phys. Rev. B **86**, 144112 (2012).
[72]A. Pimenov, A. A. Mukhin, V. Yu. Ivanov, V. D. Travkin, A. M. Balbashov, and A. Loidl, Nat. Phys. **2**, 97 (2006).
[73]A. Pimenov, A. M. Shuvaev, A. A. Mukhin, and A. Loidl, J. Phys.: Condens. Matter **20**, 434209 (2008).
[74]D. Senff, N. Aliouane, D. N. Argyriou, A. Hiess, L. P. Regnault, P. Link, K. Hradil, Y. Sidis, and M. Braden, J. Phys.: Condens. Matter **20**, 434212 (2008).
[75]N. Kida, Y. Takahashi, J. S. Lee, R. Shimano, Y. Yamasaki, Y. Kaneko, S. Miyahara, N. Furukawa, T. Arima, and Y. Tokura, J. Opt. Soc. Am. B **26**, A35 (2009).
[76]A. Pimenov, A. Shuvaev, A. Loidl, F. Schrettle, A. A. Mukhin, V. D. Travkin, V. Yu. Ivanov, and A. M. Balbashov, Phys. Rev. Lett. **102**, 107203 (2009).
[77]A. M. Shuvaev, V. D. Travkin, V. Yu. Ivanov, A. A. Mukhin, and A. Pimenov, Phys. Rev. Lett. **104**, 097202 (2010).
[78]A. B. Sushkov, R. Valdés Aguilar, S. Park, S-W. Cheong, and H. D. Drew, Phys. Rev. Lett. **98**, 027202 (2007).
[79]S. Pailhès, X. Fabrèges, L. P. Régnault, L. Pinsard-Godart, I. Mirebeasu, F. Moussa, M. Hennion, and S. Petit, Phys. Rev. B **79**, 134409 (2009).
[80]M. Cazayous, Y. Gallais, A. Sacuto, R. de Sousa, D. Lebeugle, and D. Colson, Phys. Rev. Lett. **101**, 037601 (2008).
[81]P. Rovillain, R. de Sousa, Y. Gallais, A. Sacuto, M. A. Méasson, D. Colson, A. Forget, M. Bibes, A. Barthélémy, and M. Cazayous, Nature Mater. **9**, 975 (2010).
[82]N. Kida, D. Okuyama, S. Ishiwata, Y. Taguchi, R. Shimano, K. Iwasa, T. Arima, and Y. Tokura, Phys. Rev. B **80**, 220406(R) (2009).
[83]N. Kida, S. Kumakura, S. Ishiwata, Y. Taguchi, and Y. Tokura, Phys. Rev. B **83**, 064422 (2011).
[84]S. Seki, N. Kida, S. Kumakura, R. Shimano, and Y. Tokura, Phys. Rev. Lett. **105**, 097207 (2010).
[85]I. Kézsmárki, N. Kida, H. Murakawa, S. Bordács, Y. Onose, and Y. Tokura, Phys. Rev. Lett. **106**, 057403 (2011).
[86]A. Shuvaev, F. Mayr, A. Loidl, A. A. Mukhin, and A. Pimenov, Eur. Phys. J. B **80**, 351 (2011).
[87]R. Schleck, R. L. Moreira, H. Sakata, and R. P. S. M. Lobo, Phys. Rev. B **82**, 144309 (2010).
[88]T. Kimura, T. Goto, H. Shintani, K. Ishizaka, T. Arima, and Y. Tokura, Nature (London) **426**, 55 (2003).
[89]N. Matsumoto, T. Fujii, K. Kageyama, H. Takagi, T. Nagashima, and M. Hangyo, Jpn. J. Appl. Phys. **48**, 09KC11 (2009).
[90]N. Matsumoto, T. Hosokura, T. Nagashima, and M. Hangyo, Opt. Lett. **36**, 265 (2011).
[91]M. Neshat and N. P. Armitage, Opt. Express **20**, 29063 (2012).